

Scanning diffracted-light microscopy

HIRA FAROOQ,^{1,2,*} SUELI SKINNER-RAMOS,^{1,2} HAWRA ALGASHAM,^{1,2} AYRTON A. BERNUSI,^{2,3}
AND LUIS GRAVE DE PERALTA^{1,2}

¹Department of Physics and Astronomy, Texas Tech University, Lubbock, Texas 79409, USA

²Nano Tech Center, Texas Tech University, Lubbock, Texas 79409, USA

³Department of Electrical and Computer Engineering, Texas Tech University, Lubbock, Texas 79409, USA

*Corresponding author: hira.farooq@ttu.edu

Received 22 June 2018; revised 7 August 2018; accepted 7 August 2018; posted 8 August 2018 (Doc. ID 335905); published 29 August 2018

Scanning the direction of the light that is diffracted by a sample permits the achievement of image diversity, which is necessary for implementing the Fourier ptychographic microscopy technique (FPM) using only perpendicular illumination. We also demonstrated that the same method allows for implementation of the illumination-direction-multiplexing FPM technique when the sample is illuminated using a ring-shaped condenser. © 2018 Optical Society of America

OCIS codes: (180.0180) Microscopy; (110.2990) Image formation theory; (110.2945) Illumination design.

<https://doi.org/10.1364/AO.57.007329>

1. INTRODUCTION

Image diversity is an important requirement for a successful implementation of the Fourier ptychographic microscopy (FPM) technique [1,2]. FPM is based on the collection of several low-resolution images obtained by illuminating the sample from different directions [1–5]. FPM is a phase-recovery imaging technique [6–14] that can produce images with a resolution better than the Rayleigh resolution limit $\lambda/(2NA_o)$, where λ is the wavelength in a vacuum of the light used for imaging, and NA_o is the numerical aperture of the microscope's objective lens [1,3]. Originally, FPM was first developed assuming that the incident illumination originates from a single direction at a time [1–5]. This may be very time-consuming since several images need to be collected. A natural solution to speed up the process was to illuminate the sample simultaneously from multiple directions; as such, a FPM phase-recovery algorithm capable of illumination-direction-multiplexing (IDM) was recently demonstrated [15–17]. Nevertheless, the required number of images of the sample in IDM-FPM cannot be reduced to 1 because some image diversity is still necessary for the IDM-FPM numeric algorithm to successfully converge [16]. FPM has also been implemented for macroscopic imaging using a single direction of illumination [18]. In this case, the required image diversity was obtained by taking several pictures of the sample through a translating circular aperture placed in the Fourier plane (FP) of the optical system [18]. The first contribution of this work to the growing body of research dedicated to the FPM technique consists of the demonstration of a practical method for implementing FPM using a single direction of illumination. We used a rotating slit placed at the back focal plane of the microscope's objective lens for

scanning the direction of the light diffracted by the sample. We denote this technique scanning diffracted-light microscopy (SDLM). In SDLM, the light used for imaging is the light diffracted by the sample that passes through the slit; therefore, the required image diversity is achieved because, in general, images obtained at different slit orientations are different. In this sense, SDLM is similar to other non-interferometric quantitative-phase imaging techniques based on pupil engineering and asymmetric imaging procedures [19–21]. For instance, in the pupil modulation differential phase contrast imaging technique, the phase of the complex field is extracted using a numerical non-iterative deconvolution algorithm from a set of different intensity images obtained by introducing different asymmetric filters in the FP of the optical system [19]. In general, the deconvolution algorithm used in these techniques depends on the number of collected images. In contrast, the FPM-like reconstruction algorithm used in SDLM is independent of the number of used images. We also implemented, using a rotating slit, an IDM-SDLM technique suitable for a microscope-condenser arrangement that is ubiquitous in biomedical labs. This is notable because it is known that the IDM-FPM algorithm fails when the illumination source produces hollow cones of light [17]. A proof-of-concept demonstration of IDM-SDLM using a ring-shaped condenser is presented. It should be noted that the IDM-SDLM technique, demonstrated here for the first time to our knowledge, is different than a less-precise microscopy technique recently reported, which also uses a rotating slit and a ring-shaped condenser [22]. In Ref. [22], it was assumed that there is a one to two correspondence between the orientation of the slit and the direction of illumination; i.e., it was assumed that only two opposite

illumination directions coming from the ring-shaped condenser illuminate the sample and pass through the slit at each slit orientation [22]. It is a good approximation for imaging simple periodic structures and low-scattering samples. In contrast, IDM-SDLM assumes that, for any slit orientation, light scattered by the samples that pass through the slit comes from all the illumination directions contained in a hollow cone of light produced by the ring-shaped condenser. This is a general and precise description of the scattering phenomenon under IDM. The two sets of proof-of-concept experiments presented in this work, in combination with previously reported experiments [18], can be considered special cases of a general SDL imaging technique where scanning the direction of the light diffracted by the sample in different ways permits the implementation of a FPM-like technique using a fixed illumination pattern. The FP of the optical instrument can be scanned in multiple ways, and the scanned aperture may have a variety of shapes. The fixed illumination pattern may be perpendicular illumination, a hollow cone of light, or any other illumination distribution. Therefore, the general SDL imaging technique is highly flexible and could be optimized for different applications. The rest of this paper is organized in the following manner. In Section 2 we describe the sample, the experimental arrangements used in this work, and the experimental images obtained. We conducted two sets of proof-of-concept experiments designed to demonstrate first, that the SDLM technique provides the required image diversity for imaging the unmeasured phase of the light field when the sample is illuminated from a single direction, and second, that the IDM-SDLM permits us to obtain images with a resolution better than the Rayleigh resolution limit when the sample is illuminated by a ring-shaped condenser. In Section 3, we describe the SDLM algorithm and discuss some SDLM simulations. In Section 4, we describe the IDM-SDLM algorithm and conduct a full IDM-SDLM simulation of the IDM experiments described in Section 2. Then, in Section 5, we present the results obtained after processing the experimental images with the numerical algorithms discussed in Sections 3 and 4. Finally, the conclusions of this work are presented in Section 6.

2. EXPERIMENTS

Figure 1 shows a schematic illustration of the experimental setup. We used a Nikon Eclipse Ti inverted microscope. As Fig. 1(a) shows, we attached two charge-coupled device (CCD) cameras to obtain real-plane (RP) and FP images of the sample. A band-pass spectral filter centered at $\lambda = 570$ nm wavelength with a 10 nm bandwidth was inserted next to the objective lens to select a narrow frequency band of the diffracted light.

We perform two sets of proof-of-concept experiments. In the first set of experiments, a $NA_o = 0.85$ objective lens was used, and the sample was a 600 lines/mm Ronchi ruling grating with a period $p = 1.67$ μm . The sample was perpendicularly illuminated by a collimated beam of white light produced by the microscope's built-in illumination source (not shown in Fig. 1). The objective lens was chosen with a relatively large numerical aperture to emphasize the fact that the goal of the first proof-of-concept experiment is not to improve the resolution of the optical system but rather to demonstrate the SDLM's capability for retrieving the phase of the light field.

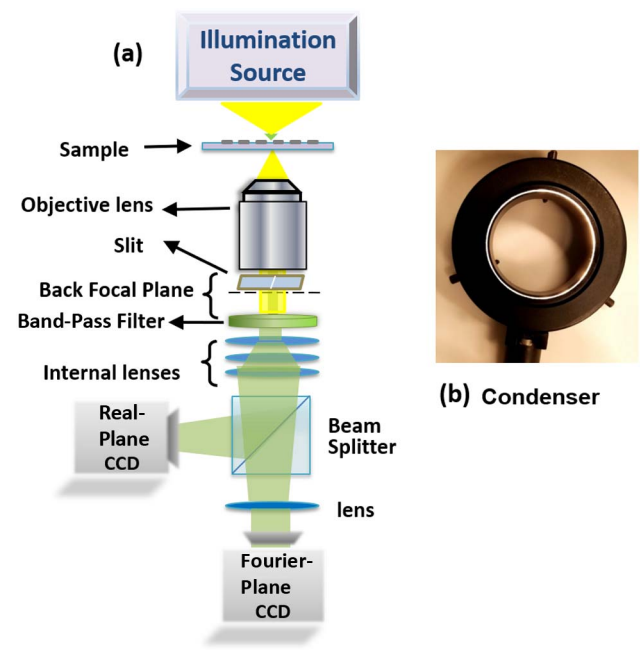


Fig. 1. (a) Schematic illustration of the experimental setup. (b) Photograph of the ring-shaped condenser.

In the second set of experiments, a ring-shaped condenser and a $NA_o = 0.15$ objective lens were used. Figure 1(b) shows a photograph of the ring-shaped, white-light-emitting condenser with an inner diameter of 5 cm used to illuminate the sample, which also was a 600 lines/mm Ronchi ruling grating with a period $p = 1.67$ μm . By changing the height of the condenser with respect to the sample, we adjusted its numerical aperture to $NA_c = 0.4 > NA_o$. Under these conditions, $p < \lambda/(2NA_o) = 1.9$ μm but $p > \lambda/(NA_o + NA_c) \sim 1.04$ μm , which is the theoretical resolution limit of the high-resolution RP image that can be obtained by processing the low-resolution RP images using the FPM algorithm [1,3]. Therefore, the goal of the second proof-of-concept experiment is to demonstrate that IDM-SDLM improves the resolution of the optical system like FPM does. Since the sample's patterned structure was not visible, a mark was introduced across the patterned structure to create a large feature to help to focus the microscope's objective lens at the sample's surface. On both set of experiments, as sketched in Fig. 1(a), a slit of a width $W_s = 0.1$ in numerical aperture units (NA), was placed in the back focal plane of the objective lens for selecting the direction of the light diffracted by the sample that was used for imaging. The rectangular shape of the slit was selected for practical reasons. It may be possible that an elongated aperture with a different shape could produce better results. There is then room for further improvements using pupil engineering methods. We took nine pairs of FP–RP images corresponding to different slit orientations. It should be noted that like FPM, SDLM only uses experimental RP images. We used the experimental FP images for extracting information and for explanation. We changed the slit orientation from 0° to 180° with a 20° angle increment, where the zero-degree angle orientation corresponds to the slit oriented perpendicularly to the direction of the slits in the Ronchi

ruling. The increment angle value was chosen to guarantee that the regions of the FP sampled by the slit, in two consecutive orientations in the second set of experiments, have sufficient (~80%) overlapping to achieve a successful convergence of the numerical algorithm [1]. The angle increment was the same in both experiments, but the slit length, NA_o , was different; therefore, the overlapping between the regions of the FP sampled by the slit, in two consecutive orientations in the first set of experiments, was smaller (~30%). The consequences of this will be discussed in Section 3. The camera exposition time was 800 ms, but it was not optimized, and the slit was rotated manually; therefore, the image acquisition process can be further improved. Figure 2 shows representative pairs of FP–RP images obtained with the experimental setup sketched in Fig. 1. The FP–RP image pairs in Fig. 2 were obtained by taking images with perpendicular illumination [Figs. 2(a)–2(d)] and with the sample illuminated by the hollow cone of light produced by the ring-shaped condenser shown in Fig. 1(b) [Figs. 2(e)–2(j)]. The ring-shaped out-of-focus objects present in Figs. 2(b) and 2(d) are dust particles present on top of the sample. They are not relevant to the discussion presented below. The elongated object visible in Figs. 2(f), 2(h), and 2(j) is the sample’s scratch used for focusing.

Figures 2(a)–2(d) show two instances of the nine FP [Figs. 2(a) and 2(c)] and RP [Figs. 2(b) and 2(d)] pairs of images obtained during the first set of experiments. The pair of FP–RP images shown in Figs. 2(a) and 2(b) were obtained with the slit oriented at $\Theta = 0^\circ$; i.e., with the slit oriented perpendicularly to the lines present in the Ronchi ruling. Zero-, first-, and second-order diffraction spots, separated by a distance $\lambda/p = 0.34 \text{ NA}$, are clearly observed in the FP image shown in Fig. 2(a); correspondingly, the periodicity of the sample is clearly seen in the RP image shown in Fig. 2(b). This is expected because $p = 1.67 \text{ }\mu\text{m} > \lambda/NA_o \sim 0.7 \text{ }\mu\text{m}$. The pair of FP–RP images shown in Figs. 2(c) and 2(d) were obtained with the slit oriented at $\Theta = 40^\circ$. Zero- and first-order diffraction spots are clearly seen in the FP image shown in Fig. 2(c);

however, the second-order diffraction spots are absent because the light producing them is blocked by the slit when it is oriented at $\Theta = 40^\circ$. Nevertheless, the periodicity of the sample is clearly seen in the RP image shown in Fig. 2(d) because the presence of at least two consecutive diffraction order spots allows for the sample’s periodicity to be visible in the corresponding RP image. Figures 2(e)–2(j) show three instances of the nine FP [Figs. 2(e), 2(g), and 2(i)] and RP [Figs. 2(f), 2(h), and 2(j)] pairs of images obtained during the second set of experiments with the slit oriented to the angles $\Theta = 20^\circ, 0^\circ, 160^\circ$, respectively. As expected, the mark introduced in the sample is seen in all the three IDM low-resolution RP images stated above, but in none of the RP experimental images is the periodic structure of the sample visible because $p < \lambda/(2NA_o)$. When a periodic sample is illuminated by a hollow cone of light, diffraction rings with a radius of NA_c are observed in the FP images [23,24]. However, only a fraction of a ring is visible when a slit is introduced in the back focal plane of the objective lens. In excellent correspondence, in the three FP images shown in Figs. 2(e), 2(g), and 2(i), two small bright arcs corresponding to first-order diffraction rings can be seen, but the zero-order diffraction ring is not visible because $NA_c = 0.4 > NA_o = 0.15$. A comparison of Figs. 2(e), 2(g), and 2(i) reveals that the visible arc in these figures seems to rotate, describing a ring when the slit is rotated.

3. SDLM ALGORITHM AND SIMULATIONS

Figure 3 shows a schematic illustration of the SDLM algorithm flowchart, which is similar to the FPM algorithm [1–5].

The phase of the optical disturbance (OD) at the microscope’s RP is lost during the measurement in the camera [25]; however, as it is shown below, the SDLM algorithm permits the recovery of the unmeasured phase from a set of RP images obtained as described in Section 2, i.e., using perpendicular illumination while taking each image at a different slit orientation. As shown in block (1) of Fig. 3, the SDLM algorithm starts

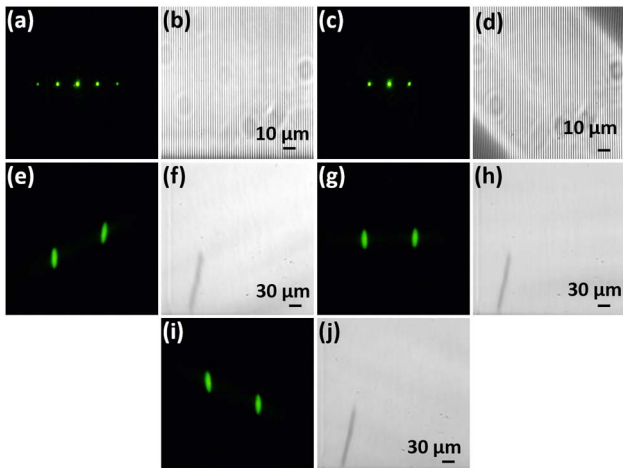


Fig. 2. Examples of experimental pairs of (a), (c), (e), (g), (i) FP and (b), (d), (f), (h), (j) RP images obtained using (a)–(d) perpendicular illumination and (e)–(j) the ring-shaped condenser, with the slit rotated counterclockwise by (a), (b) and (g), (h) 0° , (e), (f) 20° , (c), (d) 40° , and (i), (j) 160° .

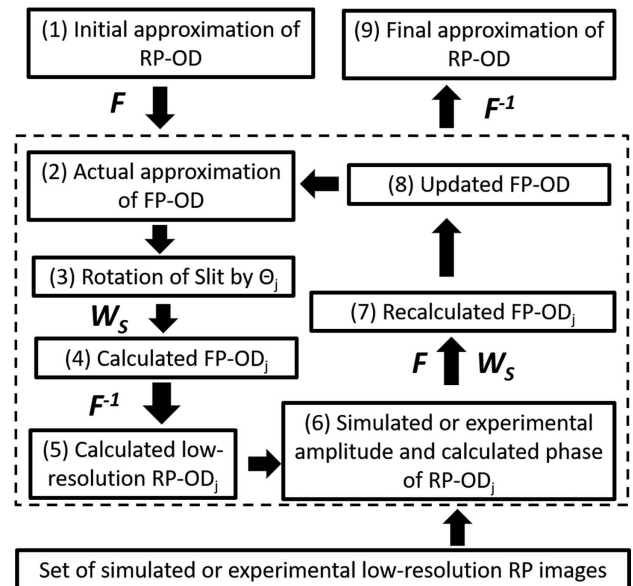


Fig. 3. SDLM algorithm flowchart.

assuming some initial approximation ($m = 0$) for the amplitude $[a_{m=0}(r)]$ and phase $[p_{m=0}(r)]$ of the RP-OD. Then, as shown in block (2) of Fig. 3, the first actual approximation ($m = 1, j = 1$) of the FP-ODs is calculated by applying a two-dimensional (2D) Fourier transform operation (F) [1–5],

$$A_{m,j}^{\text{act}}(k)e^{ip_{m,j}^{\text{act}}(k)} = F[a_{m=0}(r)e^{ip_{m=0}(r)}]. \quad (1)$$

In Eq. (1), r and k are 2D vectors defined in the RP and FP, respectively. A rectangular window $W_S(\Theta_j)$, corresponding to the physical slit placed at the objective focal plane as shown in Fig. 1, is defined in the FP with length NA_o , width W_s , and centered at $k = 0$. As shown in block (3) of Fig. 3, the rectangular window is then rotated with respect to $k = 0$ at an angle Θ_j . Then, as shown in block (4) of Fig. 3, Eq. (2) is used to calculate the first approximation to the amplitude $[A_{m=1,j=1}(k)]$ and phase $[P_{m=1,j=1}(k)]$ corresponding to the FP image that would be observed when the slit is oriented at angle Θ_j ,

$$A_{m,j}(k)e^{ip_{m,j}(k)} = A_{m,j}^{\text{act}}(k)e^{ip_{m,j}^{\text{act}}(k)} \cdot W_S(\Theta_j). \quad (2)$$

Then, as shown in block (5) of Fig. 3, the amplitude $[a_{m,j}(r)]$ and phase $[p_{m,j}(r)]$ corresponding to the related RP image are calculated by applying a 2D inverse Fourier transform operation (F^{-1}) [1–5],

$$a_{m,j}(r)e^{ip_{m,j}(r)} = F^{-1}[A_{m,j}(k)e^{ip_{m,j}(k)}]. \quad (3)$$

As shown in block (6) of Fig. 3, like in FPM [1–5], in SDLM the calculated amplitude of the RP image $[a_{m,j}(r)]$ is substituted by the amplitude of the corresponding experimental or simulated RP image $[a_j(r)]$. Then, as shown in block (7) of Fig. 3, the amplitude and phase corresponding to the FP image that would be observed when the slit is oriented at angle Θ_j is recalculated using the following equation:

$$A_{m,j}^{\text{rec}}(k)e^{ip_{m,j}^{\text{rec}}(k)} = F[a_j(r)e^{ip_{m,j}(r)}] \cdot W_S(\Theta_j). \quad (4)$$

Equations (2) and (4) are different in the FPM algorithm; therefore, using Eqs. (2) and (4) is a distinctive feature of the SDLM algorithm. In SDLM image diversity is achieved by rotating the slit, but in FPM it is achieved by changing the illumination direction. Next, as shown in block (8) of Fig. 3, the updated approximation of the FP-OD is calculated by adding a weighted difference between the calculated and recalculated FP-ODs, obtained for the slit orientation Θ_j , to the actual approximation of the FP-OD given by Eq. (1); i.e., using Eq. (5) [1–5],

$$A_{m,j}^{\text{upd}}(k)e^{ip_{m,j}^{\text{upd}}(k)} = A_{m,j}^{\text{act}}(k)e^{ip_{m,j}^{\text{act}}(k)} + \alpha[A_{m,j}^{\text{rec}}(k)e^{ip_{m,j}^{\text{rec}}(k)} - \gamma A_{m,j}(k)e^{ip_{m,j}(k)}]. \quad (5)$$

In this work, all simulation results were obtained using $\alpha = \beta = \gamma = 1$, while $\alpha = 0.8$, $\beta = 0.5$, and $\gamma = 0.8$ were the values used when processing experimental images. As indicated by the arrows between blocks (8) and (2) of Fig. 3, after the initial approximation of the FP-OD is updated, the updated FP-OD is used as the actual approximation ($j = 2$). The operations included in the box with a discontinuous line in Fig. 3 are successively done for each slit orientation (indicated by the sub-index j). This constitutes the first iteration ($m = 1$) in the SDLM algorithm, and the algorithm should converge after several iterations. Finally, as shown in block (9) of Fig. 3, the 2D Fourier

transform of the FP-OD gives the final RP-OD. We performed a full simulation of the first set of experiments described in Section 2 using nine previously simulated RP images, which correspond to the nine experimental RP images obtained with the experimental setup sketched in Fig. 1 but illuminate the sample with the collimated white-light beam produced by the built-in microscope's illumination source. The simulated RP images were calculated assuming an OD at the sample's plane with amplitude and phase with the known periodicity of the sample plus 3% of additive (uniform) random intensity and phase noise. This is followed by using Eqs. (1)–(3), as indicated by blocks (1)–(5) in Fig. 3. Then, the simulated RP images were calculated as the intensities corresponding to the calculated RP-ODs. We assumed that a slit with $W_s = 0.1$ was rotated from $\Theta = 0^\circ$ to 180° at intervals of $\Delta\Theta = 20^\circ$. $W_s = 0.1$ guarantees a superposition larger than 60% between consecutive FP regions sampled by the slit inside of a circle with radius $\lambda/p = 0.34$ NA [1–3]. The SDLM algorithm starts by assuming an initial approximation of the RP-OD. As this is often chosen in FPM [1–5], we choose $p_{m=0}(r) \equiv 0$ and $a_{m=0}(r)$ as the amplitude corresponding to a low-resolution RP image obtained with the same experimental setup but without the slit. Figure 4 shows the simulation results corresponding to the first set of experiments that were obtained by processing the simulated RP images with the SDLM algorithm.

Figures 4(a) and 4(b) show, respectively, the assumed exact amplitude and phase of the RP-OD corresponding to the Ronchi ruling grating with a period $p = 1.67 \mu\text{m}$, when the sample is perpendicularly illuminated and observed with a $NA_o = 0.85$ objective lens. Figures 4(c) and 4(d) show an instance of a pair of simulated FP and RP images, respectively, which were obtained assuming the slit placed at the back focal

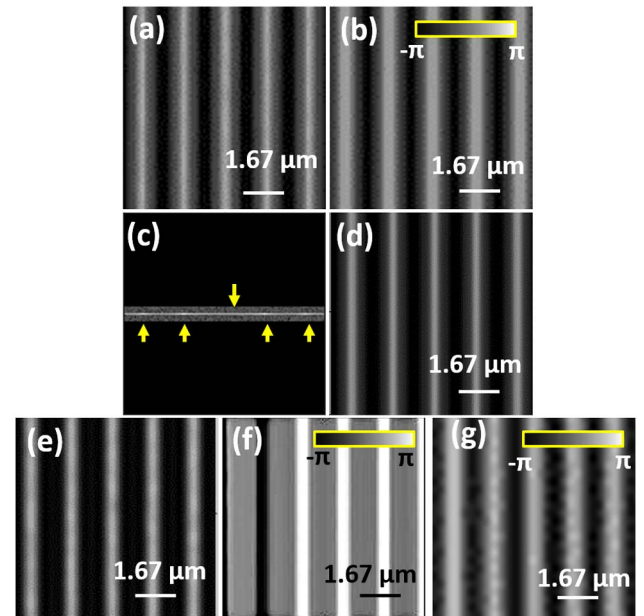


Fig. 4. SDLM simulation results. Exact (a) amplitude and (b) phase of the RP-OD. Simulated (c) FP and (d) RP images obtained with the slit oriented at $\Theta = 0^\circ$. (e) Amplitude and (f), (g) phase of the simulated RP-OD obtained after 10 iterations of the SDLM algorithm using (e), (f) 9 and (g) 20 different slit orientations.

plane of the objective lens was oriented at the angle $\Theta = 0^\circ$. As expected from $p > \lambda/\text{NA}_o$, and in correspondence with the experimental pair of FP and RP images shown in Figs. 2(a) and 2(b), several diffraction spots [pointed by arrows in Fig. 4(c)] are clearly visible in the FP images shown in Figs. 4(c) and 2(a), and the periodicity of the sample is clearly visible in the RP images shown in Figs. 4(d) and 2(b). The amplitude and phase of the RP-OD obtained by processing the nine and 20 RP simulated images, after just 10 iterations of the SDLM algorithm, are shown in Figs. 4(e)–4(g), respectively. As expected, the periodicity of the sample ($p = 1.67 \mu\text{m}$) is visible in Figs. 4(e)–4(g). Using a standard metric for quantitative comparison of the exact and simulated RP-ODs [26,27], we obtained a (square root of the mean square error) $RMS = 0.02$, which is a low value. Nevertheless, the relatively large error in the phase image shown in Fig. 4(f) is due to a suboptimal superposition of $\sim 30\%$ between the FP regions sampled by the slit in two consecutive orientations. This is confirmed by the phase image shown in Fig. 4(g), which was obtained by increasing the number of slit orientations from nine to 20. In this case, the superposition between the FP regions sampled by the slits in two consecutive orientations is $\sim 45\%$, and RMS decreases to 0.007. This suggests that SDLM should permit the recovery of the unmeasured phase of the RP-OD. In addition to making a full simulation of the first set of experiments described in Section 2, we conducted a more general simulation corresponding to an arbitrary sample illuminated with perpendicular light, which is observed with a $\text{NA}_o = 0.85$ objective lens. We assumed the same simulation parameters used before for the periodic sample. The results for this simulation are shown in Fig. 5.

Figures 5(a) and 5(b) show, respectively, the exact amplitude and phase of the RP-OD, corresponding to an arbitrary sample perpendicularly illuminated and observed with a $\text{NA}_o = 0.85$ objective lens. The amplitude and phase of the RP-OD obtained by processing nine previously simulated RP images, after 100 iterations of the SDLM algorithm, are shown in Figs. 5(c) and 5(d), respectively. A comparison between Figs. 5(d) and

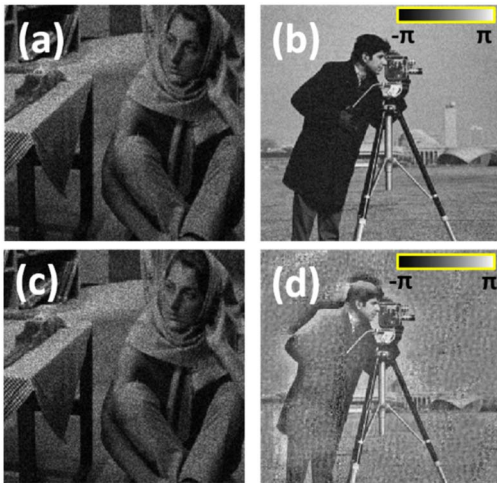


Fig. 5. SDLM simulation results for an arbitrary sample. Exact (a) amplitude and (b) phase of the RP-OD. (c) Amplitude and (d) phase of the RP-OD obtained after 100 iterations of the SDLM algorithm.

5(b) reveals that most of the principal features of the exact phase distribution are present in Fig. 5(d). A quantitative comparison between the exact and simulated RP-ODs produced an $RMS = 0.017$. This suggests that SDLM should also permit the recovery of the unmeasured phase of the RP-OD for arbitrary samples. We attribute the small phase errors in Fig. 5(d) to an insufficient number of images (nine). SDLM and IDM-SDLM numerical algorithms are very similar to FPM and IDM-SDLM ones. We found that the time needed for each iteration of the SDLM and IDM-SDLM algorithms is practically equal to the corresponding time in the FPM and IDM-SDLM algorithms. A comprehensive simulation study of the applicability of the SLD imaging algorithm for arbitrary samples will be reported by the authors elsewhere.

4. IDM-SDLM ALGORITHM AND SIMULATIONS

The IDM-SDLM algorithm is similar to the IDM-FPM one [15–17]. Figure 6 shows a schematic illustration of the IDM-SDLM algorithm flowchart that we used for making a full simulation of the second set of experiments described in Section 2.

The first three steps of the IDM-SDLM algorithm, which are represented by blocks (1), (2), and (3) in Fig. 6, are identical to the first three steps of the SDLM algorithm described in Section 3. However, similar to the IDM-FPM algorithm [15–17], the steps represented by blocks (4) to (8) and Eqs. (2)–(5) should be modified when the sample is simultaneously illuminated from N different directions defined by the FP vectors k_q , where $q = 1, 2, \dots, N$. First, as represented by block (4) of Fig. 6, not one but N FP – OD $_{j,q}$ corresponding to the same slit orientation Θ_j must be calculated, one for each direction of illumination q , using the following equation:

$$A_{m,j,q}(k)e^{iP_{mj,q}(k)} = A_{m,j}^{\text{act}}(k - k_q)e^{iP_{mj}^{\text{act}}(k - k_q)} \cdot W_S(\Theta_j). \quad (6)$$

Equation (6) should be evaluated N times for a given slit orientation Θ_j ; the actual approximation of the FP-OD should

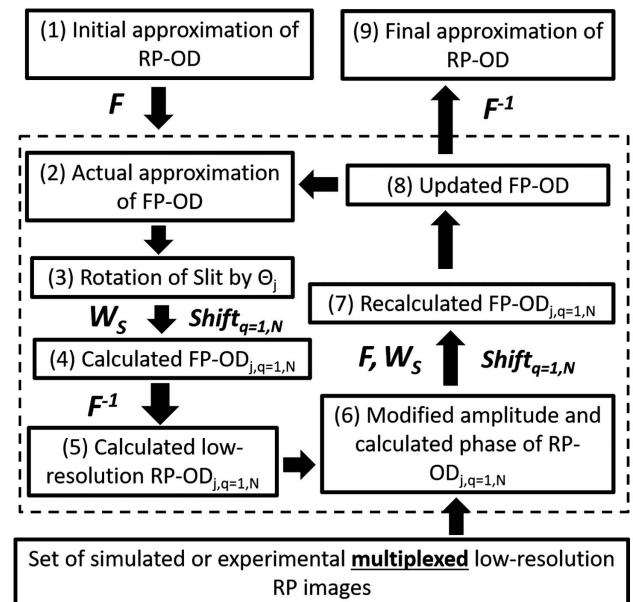


Fig. 6. IDM-SDLM algorithm flowchart.

be shifted each time by k_q and then multiplied by the rotated rectangular window $W_s(\Theta_j)$. Then, as shown in block (5) of Fig. 6, the amplitude $[a_{m,j,q}(r)]$ and phase $[p_{m,j,q}(r)]$ corresponding to each related low-resolution RP image are calculated by applying a 2D inverse Fourier transform operation (F^{-1}),

$$a_{m,j,q}(r)e^{ip_{m,j,q}(r)} = F^{-1}[A_{m,j,q}(k)e^{ip_{m,j,q}(k)}]. \quad (7)$$

At this point, as shown in block (6) of Fig. 6, similar to IDM-FPM [15–17], in IDM-SDLM, the calculated amplitude of each low-resolution RP image $[a_{m,j,q}(r)]$ is modified using the following equation:

$$a_{m,j,q}^{\text{mod}}(r) = \sqrt{\frac{I_{\text{RP},j}}{I_{\text{RPT}}}} a_{m,j,q}(r),$$

$$I_{\text{RPT}} = \sum_{q=1}^N I_{\text{RP},j,q}, \quad I_{\text{RP},j,q} = [a_{m,j,q}(r)]^2, \quad (8)$$

where $I_{\text{RP},j}$ is the intensity of the experimental (or simulated) multiplexed low-resolution RP image number j , which was obtained with the slit oriented at Θ_j . Then, as shown in block (7) of Fig. 6, each FP-OD $_{j,q}$ is recalculated using the following equation:

$$A_{m,j,q}^{\text{rec}}(k)e^{ip_{m,j,q}^{\text{rec}}(k)} = F[a_{m,j,q}^{\text{mod}}(r)e^{ip_{m,j,q}(r)}] \cdot W_s(\Theta_j). \quad (9)$$

Next, as shown in block (8) of Fig. 6, the updated approximation of the FP-OD with NA_s is calculated by adding a weighted difference between the calculated and recalculated FP-ODs with NA_o to the actual approximation of the FP-OD given by Eq. (1); i.e., using Eq. (10),

$$A_{m,j}^{\text{upd}}(k)e^{ip_{m,j}^{\text{upd}}(k)} = A_{m,j}^{\text{act}}(k)e^{ip_{m,j}^{\text{act}}(k)} + \alpha \sum_{q=1}^N [\gamma A_{m,j,q}^{\text{rec}}(k+k_q)e^{ip_{m,j,q}^{\text{rec}}(k+k_q)} - \beta A_{m,j,q}(k+k_q)e^{ip_{m,j,q}(k+k_q)}]. \quad (10)$$

The IDM-SDLM algorithm then continues as describe above for SDLM. In IDM-FPM [15–17], W_s in Eqs. (6) and (9) is independent of Θ_j ; therefore, a single IDM RP image can be obtained in IDM-FPM when using a single ring-shaped condenser. However, when using a single ring-shaped condenser for illuminating the sample, the IDM-SDLM algorithm permits us to obtain a different IDM RP image for each different value of Θ_j . We performed a full simulation of the second set of experiments described in Section 2 using nine pairs of simulated IDM FP–RP images, which correspond to the experimental images obtained with the experimental setup sketched in Fig. 1(a), where the sample was illuminated by the ring-shaped condenser shown in Fig. 1(b). The hollow cone of light produced by the condenser was approximated by $N = 36$ discrete sources of planar waves forming a ring with $\text{NA}_c = 0.4$. As in SDLM, we could start the IDM-SDLM algorithm by assuming an initial approximation of the RP-OD by choosing $p_{m=0}(r) \equiv 0$ and $a_{m=0}(r)$ as the amplitude corresponding to a low-resolution RP image obtained without the slit. However, when illuminating a sample containing a periodic structure with a ring-shaped condenser, a better RP-OD initial approximation can be obtained by extracting the information contained in the experimental (or simulated)

IDM FP images using the so-called FP imaging microscopy (FPIM) technique [23,24]. Therefore, we constructed the initial approximation of the RP-OD with $p_{m=0}(r) \equiv 0$ and $a_{m=0}(r)$, given by the following expression [22]:

$$a_{m=0}(r) = c_1 \sqrt{I_{\text{RP},\perp}} + c_2 \sqrt{I_{\text{FPIM}}}, \quad (11)$$

where c_1 and c_2 are arbitrary constants, I_{FPIM} is the intensity of the RP image that could be obtained by processing the experimental FP images using the FPIM technique [23,24], and $I_{\text{RP},\perp}$ is the intensity of a RP image obtained with the experimental setup sketched in Fig. 1, but without the slit and illuminating the sample with the collimated white light beam produced by the built-in microscope's illumination source. Therefore, when $c_2 = 0$, Eq. (11) corresponds to the initial approximation used in SDLM. As shown in Fig. 7, FPIM permits us to detect periodic structures with periods smaller than the Rayleigh resolution limit by extracting useful information present in the experimental FP images [23,24].

The simulated IDM images were calculated assuming an OD with amplitude and phase with the known periodicity of the sample, followed by using Eqs. (1), (6), and (7), as indicated by blocks (1) to (5) in Fig. 6. Then the simulated IDM FP and RP images $[I_{\text{RPT}}$ in Eq. (8)] were calculated as the sum of the intensities corresponding to the $N = 36$ calculated FP- and RP-ODs $[I_{\text{RP},j,q}$ in Eq. (8)]. Figures 7(a) and 7(b) show two instances of simulated IDM FP images corresponding to the slits oriented at $\Theta_j = 160^\circ$ and 20° , respectively. As expected, they match well with the experimental IDM FP images

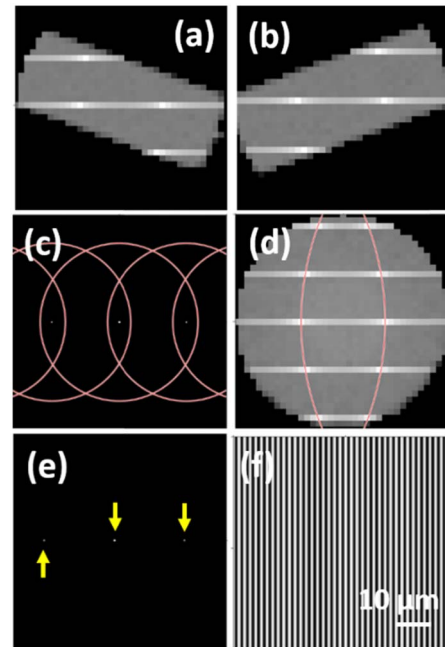


Fig. 7. (a), (b) Instances of simulated IDM FP images corresponding to $\Theta_j =$ (a) 160° and (b) 20° . (c)–(f) Results obtained after processing the nine simulated IDM FP images of the sample with $p = 1.67 \mu\text{m}$ using the FPIM technique. (c) Diffraction rings of radii equal to $\text{NA}_c = 0.4$, (d) superposition of the sum of all the simulated IDM FP images and the first-order diffraction rings, (e) respective centers of the diffraction rings separated by a distance $\lambda/p = 0.34$, and (f) I_{FPIM} .

shown in Figs. 2(i) and 2(e). Similar to the experimental IDM FP images shown in Figs. 2(e), 2(g), and 2(i), the simulated IDM FP images seem to rotate, forming a ring with a radius $NA_c = 0.4$ when the slit rotates. As shown in Fig. 7(c), the FPIM technique allows us to reconstruct the zero- and higher-order diffraction rings that would be formed in the microscope's FP when the sample is illuminated by a microscope condenser emitting a hollow cone of light [23,24]. The two solid arcs observed in Fig. 7(d) perfectly overlap with the dotted arcs, which are obtained by adding all the simulated IDM FP images. These arcs are the portions of the first-order diffraction rings with radii equal to NA_c that can be observed with the $NA_o = 0.15$ objective lens. Figure 7(e) shows the centers of the zero- and first-order diffraction rings separated by a distance $\lambda/p = 0.34 NA$. Figure 7(e) represents the amplitude of the diffraction pattern observable under perpendicular illumination with an objective lens with synthetic numerical aperture $NA_s = NA_o + NA_c = 0.55$. Figure 7(f) shows I_{FPIM} , which is obtained by taking the Fourier transform of Fig. 7(e). It is worth noting that I_{FPIM} contains the periodicity of the sample, as clearly seen in Fig. 7(f), but it is not properly an image of the sample because FPIM is not an imaging technique but a detection one [22]. Figure 8 shows the simulation results corresponding to the second set of experiments that were obtained by processing the nine simulated low-resolution IDM RP images with the IDM-SDLM algorithm and using Eq. (11), with I_{FPIM} as shown in Fig. 7(f), as the initial approximation of the RP-OD.

Figures 8(a) and 8(b) show, respectively, the assumed exact amplitude and phase of the RP-OD corresponding to a Ronchi ruling grating with a period $p = 1.67 \mu\text{m}$, which would be observed using a hypothetical objective lens with a synthetic numerical aperture $NA_s = NA_o + NA_c = 0.55$ when the sample is perpendicularly illuminated. Figure 8(c) shows the FP region that is sampled by the slit, placed at the back focal plane of the objective lens, when it is oriented at the angle $\Theta = 0^\circ$. As shown in Fig. 8(c), this region is formed by a set of $N = 36$ rectangles with a length equal to $NA_o = 0.15$ and a width $W_s = 0.1NA$. The rectangles are centered at the illumination directions $k_q, q = 1, 2, \dots, N$, forming a ring of radius $NA_c = 0.4$. When the slit is rotated by an angle Θ_j , each one of the rectangles is rotated about its center with the same angle (not shown). Figure 8(d) shows an instance of a simulated low-resolution IDM RP image, which was obtained assuming the slit was placed at the back focal plane of the objective lens and oriented at the angle $\Theta = 0^\circ$. As expected, and in correspondence with the experimental low-resolution IDM RP image shown in Fig. 2(h), the periodicity of the sample is not visible in Fig. 8(d) because $p = 1.67 \mu\text{m} < \lambda/(2NA_o)$. The amplitude and phase of the RP-OD obtained by processing the nine simulated low-resolution IDM RP images, after just three iterations of the IDM-SDLM algorithm, are shown in Figs. 8(e) and 8(f), respectively. A quantitative comparison between the exact and simulated RP-ODs produced an $\text{RMS} = 0.007$. A comparison between Figs. 8(e) and 8(a) and Figs. 8(f) and 8(b) suggests that IDM-SDLM should be able to surpass the Rayleigh resolution limit and should also permit us to recover the unmeasured phase of the RP-OD. The conclusions extracted from the IDM-SDLM simulation

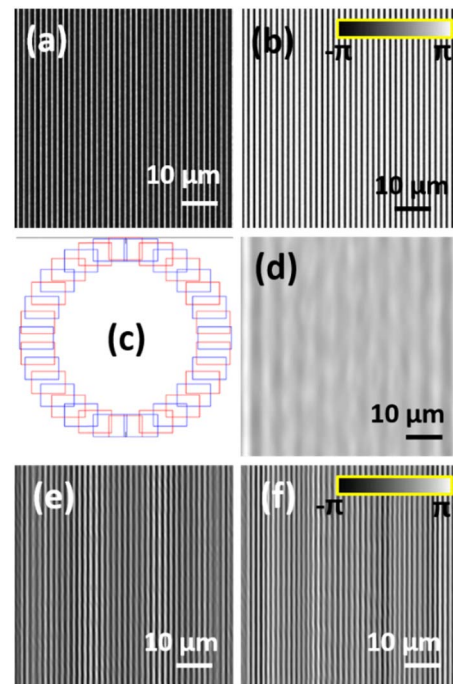


Fig. 8. IDM-SDLM simulation results. Exact (a) amplitude and (b) phase of the RP-OD. (c) Sampled region of the FP and (d) simulated IDM RP image obtained when the slit is oriented at $\Theta = 0^\circ$. (e) Amplitude and (f) phase of the simulated RP-OD obtained after three iterations of the IDM-SDLM algorithm.

results shown in Fig. 8 apply to imaging a periodic structure; however, as it will be shown below, they also apply to arbitrary samples. Moreover, a comprehensive simulation study of the IDM-SDLM algorithm addressing this point will be reported elsewhere.

5. IDM-SDLM PROCESSING OF EXPERIMENTAL IMAGES AND DISCUSSION

We processed the experimental images following the same procedure described in Sections 3 and 4 for the simulated images. The results obtained using the FPIM technique and the experimental IDM FP images, which were obtained in the second set of experiments described in Section 2, are shown in Fig. 9.

As shown in Fig. 9(a), the FPIM technique permits the construction of the diffraction rings visible in the FP images, which would be produced by a physical arrangement where a sample is illuminated with a hollow cone of light [23,24]. The radii of the diffraction rings are equal to NA_c , and their centers are separated by a distance of $\lambda/p = 0.34 NA$. The value of NA_c is obtained from the experimental IDM FP images using the FPIM technique by adding up all the experimental FP images to produce the final image shown in Fig. 9(b). The two arcs shown in Fig. 9(b) correspond to the first-order diffraction rings with radius NA_c shown in Fig. 9(a). Using this information, Fig. 9(c) is constructed containing the zero- and first-order diffraction spots (indicated by arrows) within the synthetic numerical aperture (shown by the white dashed circle). Finally, Fig. 9(d) shows the intensity corresponding to the Fourier transform of

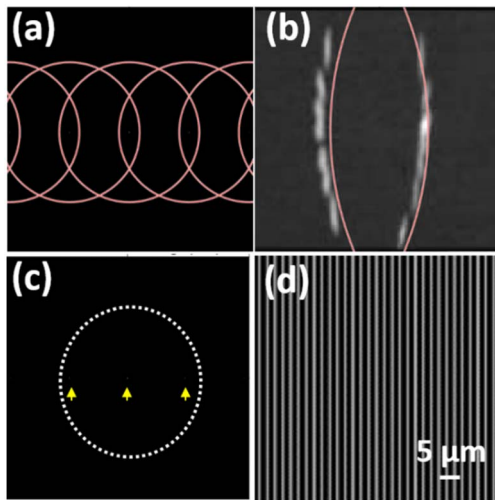


Fig. 9. Results obtained after processing with the FPIM technique the nine experimental IDM FP images obtained in the second set of experiments. (a) Diffraction rings with radii equal to $NA_c = 0.4$, (b) superposition of the sum of all FP images and the first-order diffraction rings, (c) centers of the diffraction rings separated by a distance $\lambda/p = 0.34$, and (d) amplitude square (intensity) of the Fourier transform of (c) containing a periodic structure with $p = 1.67 \mu\text{m}$.

Fig. 9(c). I_{FPIM} , obtained in this way, corresponds to a periodic structure with a period $p = 1.67 \mu\text{m}$. Figure 9(d) does not show an image of the sample because it only carries information about the periodical structure of the sample. For instance, the large scratch visible in the experimental IDM RP images shown in Figs. 2(f), 2(h), and 2(j) is not present in Fig. 9(d).

Figures 10(a)–10(c) [Figs. 10(d)–10(f)] show the results obtained after few iterations using the SDLM (IDM-SDLM) algorithm after processing the experimental RP images collected in the first (second) set of experiments described in Section 2. In the first set of experiments described in Section 2, the sample was under perpendicular illumination; accordingly, the initial approximation of the RP-OD in the SDLM algorithm was a RP image obtained with the setup sketched in Fig. 1 but in the absence of the slit. As shown in Fig. 10(a), the zero- and first-order diffraction spots are contained in the synthetic FP image of radius $NA_s = NA_o = 0.85$. From Fig. 10(a), we observed a distance of ~ 0.34 NA between the consecutive diffraction spots, which is in excellent correspondence with the expected calculated value $\lambda/p = 0.34$ NA, and with the presence of a periodic structure with $p = 1.67 \mu\text{m}$ in Figs. 10(b) and 10(c), which show the amplitude and phase of the RP-OD, respectively. A line profile corresponding to Fig. 10(b) is shown in Fig. 10(g), which corresponds to a periodic structure with $p = 1.67 \mu\text{m}$ observed with a $\sim 43\%$ contrast. A comparison between Figs. 10(b) and 10(c) and Figs. 4(e) and 4(f), respectively, reveals an excellent correspondence between the calculated RP-ODs using experimental and simulated RP images. This demonstrates that the SDLM technique successfully provides the required image diversity for the implementation of a modified version of the FPM algorithm using a single illumination direction.

In the second set of experiments described in Section 2, the sample was illuminated by a ring-shaped condenser of

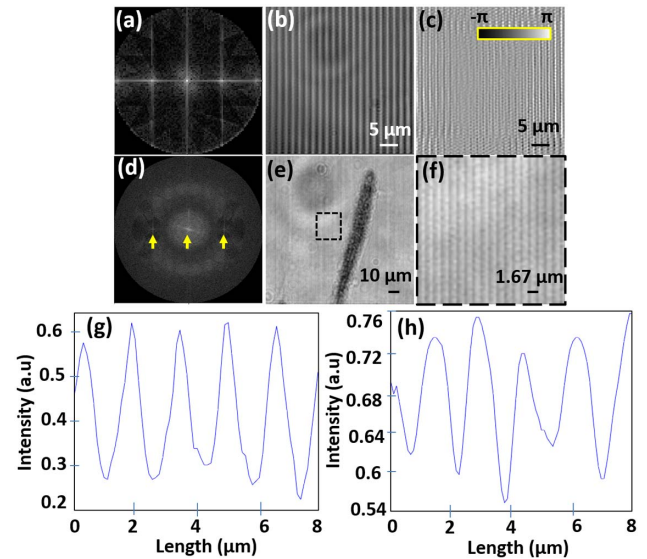


Fig. 10. Results obtained after processing the experimental RP images using the (a)–(c) SDLM and (d)–(f) IDM-SDLM algorithms. (a), (d) Synthetic FP image with $NA_s = (a) NA_o = 0.85$ and (d) $NA_o + NA_c = 0.55$. Corresponding (b), (e) intensity and (c) phase of the high-resolution RP-ODs. (f) Zoom into (e); (g) and (h) line intensity profiles obtained from (b) and (f), respectively.

$NA_c = 0.4$ shown in Fig. 1(b). Accordingly, we used Eq. (11) for constructing the initial approximation of the RP-OD in the IDM-SDLM algorithm. We used $c_1 = c_2 = 0.5$, I_{FPIM} , as shown in Fig. 9(d), and $I_{\text{RP,L}}$ was a low-resolution RP image obtained with the setup sketched in Fig. 1 but without the slit. The arrows shown in Fig. 10(d) point to the zero- and first-order diffraction spots contained in the synthetic FP image of radius $NA_s = NA_o + NA_c = 0.55$. Figure 10(e) shows the amplitude of the calculated RP-OD. From Fig. 10(d), we determined a distance between consecutive diffraction spots of ~ 0.34 NA, which is in excellent correspondence with the expected value $\lambda/p = 0.34$ NA and with the presence of a periodic structure with $p = 1.67 \mu\text{m}$ in Fig. 10(e), an inset of which is shown in Fig. 10(f). A line profile corresponding to Fig. 10(f) is shown in Fig. 10(h), which corresponds to a periodic structure with $p = 1.67 \mu\text{m}$ observed with a $\sim 15\%$ contrast. A comparison between Figs. 10(f) and 8(e) reveals an excellent correspondence between the amplitudes of the calculated RP-OD using low-resolution IDM experimental and simulated RP images, respectively. It is worth noting that the periodic structure visible in Fig. 10(f) is not visible in any of the experimental low-resolution IDM RP images, like the ones shown in Figs. 2(f), 2(h), and 2(j), because $p < \lambda/(2NA_o)$. This demonstrates IDM-SDLM can achieve image resolution values below the Rayleigh resolution limit. Moreover, the presence of the irregular-shaped scratch in Fig. 10(e) demonstrates that the IDM-SDLM technique can be applied for imaging non-periodic samples. The obtained resolution improvement is evident when comparing the image of the scratch in Fig. 10(e) with the experimental low-resolution RP images shown in Figs. 2(f), 2(h), and 2(j). The experimental setup shown in Fig. 1, but without the slit, permits us to obtain a single image of a sample illuminated by a hollow cone of light,

lacking the required image diversity for implementing the IDM-FPM algorithm. However, the results shown in Figs. 10(d)–10(f) demonstrate that the IDM-SDLM technique allows enough image diversity for implementing an IDM-FPM-like algorithm when the sample is illuminated by a hollow cone of light, which, for instance, may be produced by a ring-shaped condenser.

6. CONCLUSIONS

We implemented, simulated, and presented proof-of-concept experimental results demonstrating the SDLM and IDM-SDLM techniques. SDLM permits the implementation of the FPM algorithm using a single illumination direction, which can have applications where microscopes or telescopes are used for imaging the phase of the OD. IDM-SDLM permits the implementation of the IDM-FPM algorithm when the sample is illuminated by a single hollow cone of light. When $NA_c > NA_o$, IDM-SDLM will allow for improving the resolution of microscope-condenser arrangements that are ubiquitous in biomedical labs from $\lambda/(2NA_o)$ to $\lambda/(NA_o + NA_c)$. Moreover, when $NA_c \gg NA_o$, IDM-SLM could provide an alternative way to optically image nano-structures.

Funding. National Science Foundation (NSF) (ECCS-1404394).

REFERENCES

- G. Zheng, R. Horstmeyer, and C. Yang, "Wide-field, high-resolution Fourier ptychographic microscopy," *Nat. Photonics* **7**, 739–745 (2013).
- S. Dong, Z. Bian, R. Shiradkar, and G. Zheng, "Sparsely sampled Fourier ptychography," *Opt. Express* **22**, 5455–5464 (2014).
- X. Ou, R. Horstmeyer, G. Zheng, and C. Yang, "High numerical aperture Fourier ptychography: principle, implementation and characterization," *Opt. Express* **23**, 3472–3491 (2015).
- K. Guo, Z. Bian, S. Dong, P. Nanda, Y. Wang, and G. Zheng, "Microscopy illumination engineering using a low-cost liquid crystal display," *Biomed. Opt. Express* **6**, 574–579 (2015).
- A. Ishtiaque, M. Alotaibi, S. Skinner-Ramos, D. Dominguez, A. A. Bernussi, and L. Grave de Peralta, "Fourier ptychographic microscopy at communication wavelengths using a femtosecond laser," *Opt. Commun.* **405**, 363–367 (2017).
- D. Sayre, "Some implications of a theorem due to Shannon," *Acta Crystallogr.* **5**, 843 (1952).
- R. W. Gerchberg and W. O. Saxton, "A practical algorithm for determination of phase from image and diffraction plane pictures," *Optik* **5**, 237–250 (1972).
- J. R. Fienup, "Reconstruction of an object from the modulus of its Fourier transform," *Opt. Lett.* **3**, 27–29 (1978).
- J. R. Fienup, "Phase retrieval algorithms: a comparison," *Appl. Opt.* **21**, 2758–2769 (1982).
- H. M. L. Faulkner and J. M. Rodenburg, "Movable aperture lensless transmission microscopy: a novel phase retrieval algorithm," *Phys. Rev. Lett.* **93**, 023903 (2004).
- J. M. Rodenburg, A. C. Hurst, A. G. Cullis, B. R. Dobson, F. Pfeiffer, O. Bunk, C. David, K. Jefimovs, and I. Johnson, "Hard-X-ray lensless imaging of extended objects," *Phys. Rev. Lett.* **98**, 034801 (2007).
- M. Humphry, B. Kraus, A. Hurst, A. Maiden, and J. Rodenburg, "Ptychographic electron microscopy using high-angle dark-field scattering for sub-nanometer resolution imaging," *Nat. Commun.* **3**, 730 (2012).
- A. M. Maiden, J. M. Rodenburg, and M. J. Humphry, "Optical ptychography: a practical implementation with useful resolution," *Opt. Lett.* **35**, 2585–2587 (2010).
- A. M. Maiden, M. J. Humphry, F. Zhang, and J. M. Rodenburg, "Superresolution imaging via ptychography," *J. Opt. Soc. Am. A* **28**, 604–612 (2011).
- S. Dong, R. Shiradkar, P. Nanda, and G. Zheng, "Spectral multiplexing and coherent-state decomposition in Fourier ptychographic imaging," *Biomed. Opt. Express* **5**, 1757–1767 (2014).
- L. Tian, X. Li, K. Ramchandran, and L. Waller, "Multiplexed coded illumination for Fourier ptychography with an LED array microscope," *Biomed. Opt. Express* **5**, 2376–2389 (2014).
- M. Alotaibi, S. Skinner-Ramos, A. Alamri, B. Alharbi, M. Alfarraj, and L. Grave de Peralta, "Illumination direction multiplexing Fourier ptychographic microscopy using hemispherical digital condensers," *Appl. Opt.* **56**, 4052–4057 (2017).
- S. Dong, R. Horstmeyer, R. Shiradkar, K. Guo, X. Ou, Z. Bian, H. Xin, and G. Zheng, "Aperture-scanning Fourier ptychography for 3D refocusing and super-resolution macroscopic imaging," *Opt. Express* **22**, 13586–13599 (2014).
- S. B. Mehta and C. J. Sheppard, "Quantitative phase-gradient imaging at high resolution with asymmetric illumination-based differential phase contrast," *Opt. Lett.* **34**, 1924–1926 (2009).
- L. Tian and L. Waller, "Quantitative differential phase contrast imaging in an LED array microscope," *Opt. Express* **23**, 11394–11403 (2015).
- H. Lu, J. Chung, X. Ou, and C. Yang, "Quantitative phase-imaging and complex field reconstruction by pupil modulation differential phase contrast," *Opt. Express* **24**, 25345–25361 (2016).
- H. Farooq, S. Skinner-Ramos, H. Alghasham, and L. Grave de Peralta, "Improving the resolution of an optical microscope using ring-like illumination and scanning the direction of the diffracted light with a slit," *Opt. Commun.* **426**, 201–205 (2018).
- D. Dominguez, M. Alhusain, N. Alharbi, A. A. Bernussi, and L. Grave de Peralta, "Fourier plane imaging microscopy," *J. Appl. Phys.* **116**, 103102 (2014).
- D. Dominguez, M. Alhusain, N. Alharbi, A. A. Bernussi, and L. Grave de Peralta, "Fourier plane imaging microscopy for detection of plasmonic crystals with periods beyond the optical diffraction limit," *Plasmonics* **10**, 1337–1344 (2015).
- J. W. Goodman, *Introduction to Fourier Optics* (McGraw-Hill, 1968).
- X. Ou, G. Zheng, and C. Yang, "Embedded pupil function recovery for Fourier ptychographic microscopy," *Opt. Express* **22**, 4960–4972 (2014).
- J. R. Fienup, "Invariant error metrics for image reconstruction," *Appl. Opt.* **36**, 8352–8357 (1997).